Spin-wave cochlea and nonlocal magnetic resonance in a magnet

Hiroki Arisawa [1,2,*] Shunsuke Daimon,[2] Yasuyuki Oikawa [3] Takashi Kikkawa [2] and Eiji Saitoh[2,3,4]

[1]*Institute for Materials Research, Tohoku University, Sendai 980-8577, Japan*
[2]*Department of Applied Physics, The University of Tokyo, Tokyo 113-8656, Japan*
[3]*WPI Advanced Institute for Materials Research, Tohoku University, Sendai 980-8577, Japan*
[4]*Institute for AI and Beyond, The University of Tokyo, Tokyo 113-8656, Japan*

Spatial dependence of magnetization dynamics in a $Y_3Fe_5O_{12}$ film exposed to a magnetic-field gradient has been investigated by measuring local spin pumping and inverse spin-Hall effects. The result shows that, when microwaves are irradiated locally, magnetization precession is excited at a far distant position from the microwave irradiation position. By measuring the field and microwave frequency dependence, we found that the observed magnetization dynamics is attributed to nonlocal resonance of magnetization as well as the spatial change in the spin-wave dispersion under the magnetic-field gradient, which can be applied to realizing an innate microwave spectrometer: a spin-wave cochlea.

Our ears function as a highly sensitive spectrometer for sound waves. The key component for the sound-wave frequency resolution is a cochlea in our ears [1,2]. In a cochlea, as shown in Fig. 1(a), the local resonance frequency of sound waves is spatially modulated due to the spatial change in the elastic modulus along the spiral of the cochlea. Therefore, higher-frequency (lower-frequency) sound waves cause the maximum vibration at the inner surface of a shallower (deeper) position of the cochlea where they locally satisfy the resonance condition. By converting the vibration at different positions of the cochlea into different nerve signals, our ears distinguish sound frequencies.

In magnetic materials, collective precession motion of local magnetization propagates as waves, called spin waves [3–5]. The notable feature of spin waves is their high controllability of the resonance frequencies in terms of external magnetic fields [6–8]. Here, the controllability enables us to engineer the functionality of a cochlea into magnetic materials. By spatially modulating the resonance frequencies of spin waves by using nonuniform magnetic fields as shown in Fig. 1(b), the amplitude of spin waves with different frequencies could be enhanced at different positions.

Here, we demonstrate that a ferrimagnetic insulator $Y_3Fe_5O_{12}$ (YIG) under a magnetic-field gradient can sort spin waves by frequencies, which can be used as spin-wave and microwave spectrometers, a spin-wave cochlea. We show that the effect originates from nonlocal magnetic resonance where spin-wave excitation and resonance are spatially separated.

We excited spin waves in a YIG film (19.7 μm, 2, and 24 mm in thickness, width, and length, respectively), fabricated on a $Gd_3Ga_5O_{12}$ (111) substrate by a liquid phase epitaxy method, in a spatially modulated magnetic field. As shown in Fig. 2(a), we applied a magnetic field $\mathbf{H}(x)$ in the z direction, whose magnitude decreases almost linearly in the x direction by placing neodymium magnets ($20 \times 10 \times 5$ mm³) at the position 2 mm distant from the sample in the z direction. Here, two magnets were piled in the z direction, whose center position is $x \sim 0$, and one magnet was placed next to the magnets. Spatial distribution of $H(x)$ was measured with a Hall sensor [Fig. 2(b)], whose nonuniformity along the z direction is negligibly small (see Supplemental Material Note 1 [9]). Due to the field gradient $-\nabla H(x)$ generated from the magnets, the local resonance frequency of spin waves is modulated along the x direction in YIG. We excited spin waves by irradiating continuous microwaves with the frequency f_{MW} to the left end of the YIG slab ($x = 1$ mm) with a microwave antenna (0.1 mm in width) using a vector network analyzer (N5230C, Keysight Technologies) [Figs. 2(a) and 2(c)].

We measured spatial distribution of the spin-wave amplitude in the YIG by using the spin pumping effect [10–13] [Fig. 2(a)]; when a metal with strong spin-orbit coupling, such as Pt, is put on a magnet carrying spin waves, the spin wave injects a spin current into the metal via the spin pumping, and the injected spin current is converted into an electric voltage via the inverse spin Hall effect (ISHE) [14], enabling electrical detection of spin waves. In the present paper, three Pt films (10 nm, 2, and 1 mm in thickness, length, and width, respectively), denoted as Pt-L, Pt-C, and Pt-R films, were sputtered on the YIG slab at different center positions $x = x_L = 5.75$, $x_C = 12.25$, and $x_R = 18.75$ mm, respectively, by a radio-frequency magnetron-sputtering method. As shown in Fig. 2(c), an electric voltage V_{Pt} between the ends of each Pt film and the microwave absorption were measured with a nanovoltmeter (K2182A, Tektronix, Inc.) and the vector network analyzer, respectively. All measurements were performed at room temperature.
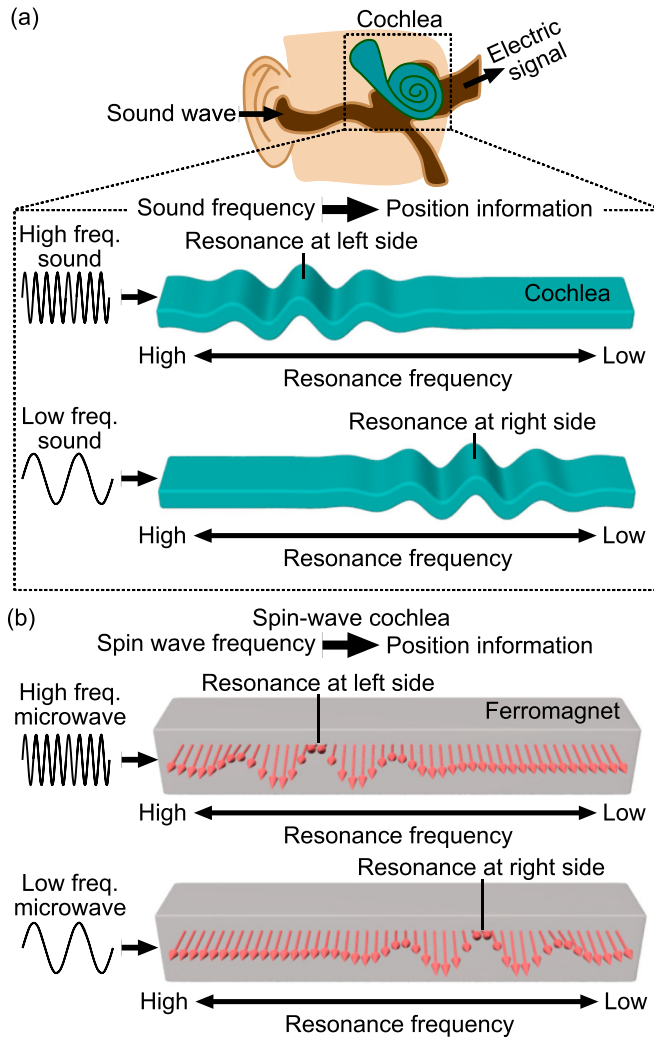
*h.arisawa@imr.tohoku.ac.jp

FIG. 1. (a) A schematic of the frequency resolution of sound waves in a cochlea. The resonance frequency of sound waves decreases along the spiral of the cochlea due to the spatial change in the elastic modulus and sound waves with different frequencies are enhanced at different positions where the sound waves locally satisfy the resonance condition. (b) A schematic of a spin-wave cochlea. Spin waves with different frequencies are enhanced at different positions due to the nonlocal resonance of spin waves under spatially nonuniform fields.

Figure 2(e) shows V_{Pt} for each Pt film at $f_{MW} = 4.770$ GHz under the magnetic-field gradient $-\nabla H \sim 13.5$ Oe mm^{-1} (average field $\bar{H} = 1013$ Oe). As shown by the red arrow, a clear V_{Pt} voltage signal appears in the Pt-C film, whereas the values of V_{Pt} are much smaller in the Pt-L and Pt-R films. We confirmed that the V_{Pt} signal observed in the Pt-C film changes its sign when the field direction is reversed from $\mathbf{H}(x)$ to $-\mathbf{H}(x)$ (see Supplemental Material Note 2 [9]), consistent with the ISHE voltage induced by the spin pumping [15]. The result indicates that spin waves excited at $f_{MW} = 4.770$ GHz is spatially enhanced at $x \sim x_C$.

The V_{Pt} signal in the Pt-L film, located near the microwave irradiation position, is small. Nevertheless, interestingly, the clear large V_{Pt} signal appears in the Pt-C film at a far distant

position from the microwave irradiation position. This means that the microwave does not induce clear resonance motion of magnetization at the end of the YIG slab locally, but it induces large magnetization precession at a far distant position nonlocally. In the present paper we refer to the phenomenon as nonlocal magnetic resonance. By changing the value of f_{MW}, we also found that the V_{Pt} voltage appears in the Pt-L and Pt-R films at $f_{MW} = 5.080$ and $f_{MW} = 4.577$ GHz, respectively [see Figs. 2(d) and 2(f)]. The results show that propagating spin waves are nonlocally resonated with the excitation under the magnetic-field gradient and the resonated spatial position moves from $x = x_L$ to x_R with decreasing f_{MW}.

Figure 3(b) shows the detailed f_{MW} dependence of V_{Pt} for each Pt film in the field gradient $-\nabla H \sim 13.5$ Oe mm^{-1} ($\bar{H} = 1013$ Oe). As shown by the red arrows, the V_{Pt} signals appear in the Pt-L, Pt-C, and Pt-R films as clear voltage peaks at $f_{MW} = f_L$, f_C, and f_R, respectively. We also measured the f_{MW} dependence of the microwave absorption S_{MW} [Fig. 3(a)] under the same field gradient. The measured S_{MW} takes large values around $f_{MW} \sim 5.25$ GHz, corresponding to the spin-wave resonance at the microwave irradiation position ($x = 1$ mm), and the conventional spin pumping voltage appears [15] in the Pt-L film in a broad frequency range [black arrow in Fig. 3(b)]. In contrast, the value of S_{MW} is small at $f_{MW} = f_L$, f_C, and f_R, implying that spin waves are out of resonance at $x = 1$ mm in spite of the resonant spin pumping at $x = x_L$, x_C, and x_R at $f_{MW} = f_L$, f_C, and f_R, respectively. We also confirmed that the amplitude of the voltage peaks at $f_{MW} = f_L$, f_C, and f_R is proportional to the microwave power P_{MW} (see SupplementalMaterial Note 3 [9]), excluding the electric voltage induced by nonlinear spin pumping effects [16].

To discuss the origin of the voltage peaks at f_L, f_C, and f_R, we estimate the local magnetic resonance conditions at each position x. As a rough estimation, we calculated the x dependence of the ferromagnetic resonance (FMR) frequency [Fig. 3(c)] using [2],

$$f_{FMR}(x) = \frac{\gamma}{2\pi}\sqrt{[H(x) - 4\pi N_z M_s][H(x) - 4\pi N_z M_s + 4\pi M_s]}. \tag{1}$$

Here, $\gamma = 1.82 \times 10^7$ Oe^{-1}s^{-1} and $4\pi M_s = 1720$ Oe are the gyromagnetic ratio and the saturation magnetization of YIG [17]. $N_z = 9.7 \times 10^{-3}$ is the effective demagnetizing factor of the YIG slab along with the z axis, determined under the assumption that the slab is an ellipsoid with the length of 24 mm, major axis of 2 mm, and minor axis of 19.7 μm. By comparing the obtained $f_{FMR}(x)$ [black solid line in Fig. 3(c)] with (x_L, f_L), (x_C, f_C), and (x_R, f_R) [blue circle, rectangle, and triangle in Fig. 3(c), respectively] we can estimate the local spin-wave resonance condition. The value of f_I ($I = $ L, C, R) shows good agreement with that of $f_{FMR}(x_I)$ ($I = $ L, C, R).

Figures 3(e)–3(l) show the magnetic-field gradient dependence of the observed voltage peaks. We applied three different field gradients: (I) $-\nabla H = 9.4$ Oe mm^{-1} ($\bar{H} = 1008$ Oe), (II) $-\nabla H = 13.4$ Oe mm^{-1} ($\bar{H} = 966$ Oe), and (III) $-\nabla H = 15.0$ Oe mm^{-1} ($\bar{H} = 923$ Oe) to the YIG/Pt
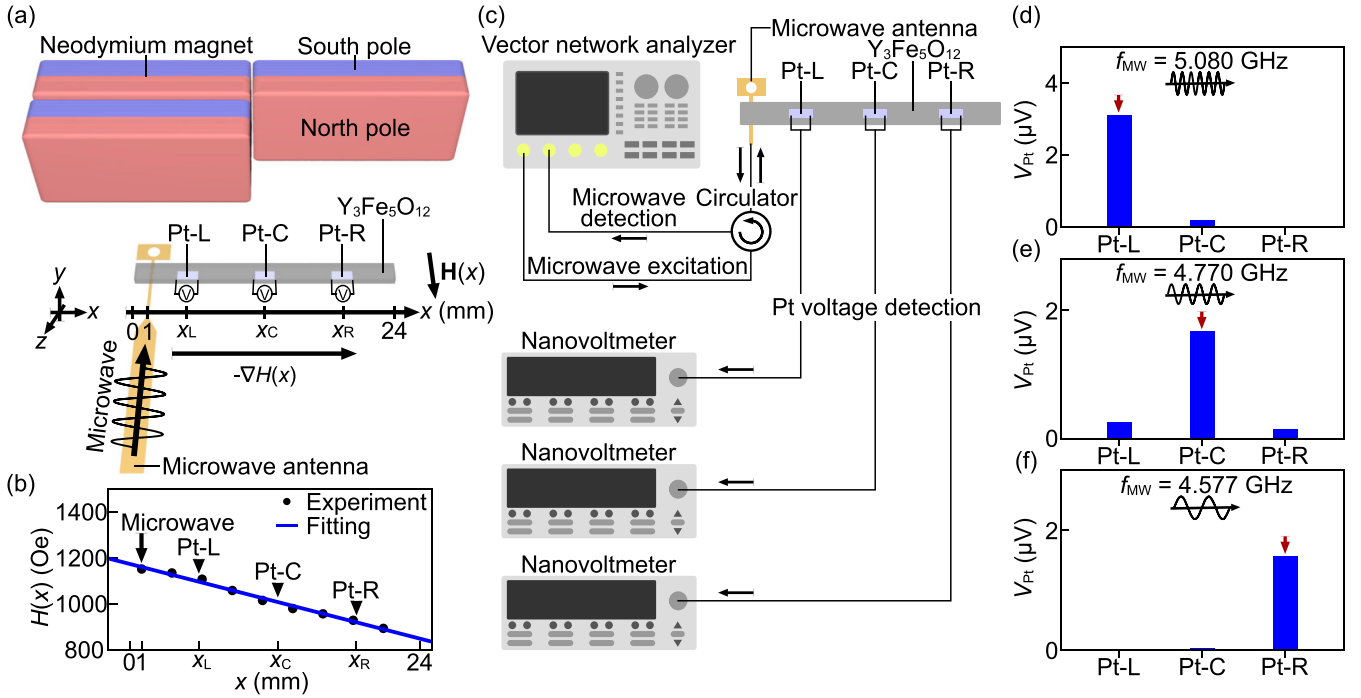
FIG. 2. (a) A measurement setup in the present paper. A magnetic field $\mathbf{H}(x)$ whose magnitude decreases along the x direction was applied in the z direction to a Pt/$Y_3Fe_5O_{12}$ (YIG) bilayer system. Spin waves were excited by irradiating continuous microwaves with the frequency f_{MW} at the bottom left end of the YIG slab ($x = 1$ mm). An electric voltage V_{Pt} in three Pt films, Pt-L, Pt-C, and Pt-R films at $x = x_L = 5.75$, $x_C = 12.25$, and $x_R = 18.75$ mm, respectively, was measured. The size of the Pt films is 10 nm, 2, and 1 mm in thickness, length, and width, respectively. (b) The spatial dependence of the intensity of the applied nonuniform magnetic field $H(x)$. Experimental data and a linear fitting are shown by the black plots and a blue solid line, respectively. The black triangles denote the center position of the Pt films. (c) A schematic of the measurement process. Microwaves were irradiated to the YIG with a vector network analyzer, and the reflected microwaves were detected with a circulator and the analyzer. V_{Pt} in each Pt film was measured by using a nanovoltmeter. (d)–(f) V_{Pt} in the Pt-L, Pt-C, and Pt-R films (d) at $f_{MW} = 5.080$ GHz, (e) $f_{MW} = 4.770$ GHz, and (f) $f_{MW} = 4.577$ GHz. The value of the microwave power P_{MW} was set to 25.1 mW.

sample [Figs. 3(f)–3(h), respectively]. Under the magnetic field gradient (I), as shown by the red arrows in Fig. 3(j), the V_{Pt} peaks appear in the Pt-L, Pt-C, and Pt-R films at different microwave frequencies $f_{MW} = f_L = 4.89$, $f_C = 4.75$, and $f_R = 4.57$ GHz, respectively. As shown in Fig. 3(k) [Fig. 3(l)], when the larger magnetic-field gradient (II) [(III)] is applied, the V_{Pt} signals appear in the Pt-L, Pt-C, and Pt-R films at $f_{MW} = f_L = 4.85$, $f_C = 4.58$, and $f_R = 4.37$ GHz ($f_L = 4.77$, $f_C = 4.40$, and $f_R = 4.21$ GHz), respectively. By comparing the voltage peaks in the Pt-I film ($I = $ L, C, R) among the three $\mathbf{H}(x)$ gradients, we found that the value of f_I ($I = $ L, C, R) shifts to the lower frequencies by applying the greater magnetic-field gradients [Figs. 3(j)–3(l)]. As shown in Fig. 3(d), the values of f_I are roughly same as those of $f_{FMR}(x_I)$ ($I = $ L, C, R) for all $\mathbf{H}(x)$ gradients, which supports our interpretation that the voltage peak appears when spin waves satisfy the local FMR condition at each position of the Pt films, filtering a particular frequency component of spin waves at a different position. The observed signal cannot be explained by the conventional spin-wave propagation in a uniform magnetic field [Fig. 3(e)], where V_{Pt} monotonically decays along the propagation direction (x direction) due to the damping of spin waves [Fig. 3(i)].

To further discuss the mechanism of the observed voltage peak, we carried out numerical calculation on the spatial distribution of spin waves in the magnetic-field gradient. As shown in Fig. 4(a), the spatially nonuniform magnetic field $\mathbf{H}_{cal}(x)$, whose amplitude linearly decreases in the x direction, was applied in the z direction to a YIG slab (20 μm, 2, and 24 mm in thickness, width, and length, respectively). The field configuration ($-\nabla H_{cal} = 9.4$ Oe mm^{-1}, average field $\overline{H_{cal}} = 1007.5$ Oe) is almost the same as the field gradient (I) in the experiment. By using mumax3 [18] we numerically calculated the temporal evolution of the magnetization $\mathbf{M}$ components at a steady precession state with applying microwave fields with the frequency f_{MWcal} at the left end of the slab ($x = 1$ mm) (see Supplemental Material Note 4 [9] for details). Figure 4(b) shows a snapshot of the spatial distribution of M_x, the x component of $\mathbf{M}$, at $f_{MWcal} = 4.70$ GHz. The magnitude of M_x is large at the position shown by the red arrow. To estimate the spin pumping voltage [4] $\propto (\mathbf{M} \times \dot{\mathbf{M}})_z$, we calculated its averaged value about z and time $\overline{(\mathbf{M} \times \dot{\mathbf{M}})_z}$ at each x [see the lower panel in Fig. 4(c)]. Here, as shown by the red arrow, $\overline{(\mathbf{M} \times \dot{\mathbf{M}})_z}$ takes its local maximum at the position $x = x_{max}$, which is determined from the Lorentzian fit (black solid curve). We also found that x_{max} decreases by increasing
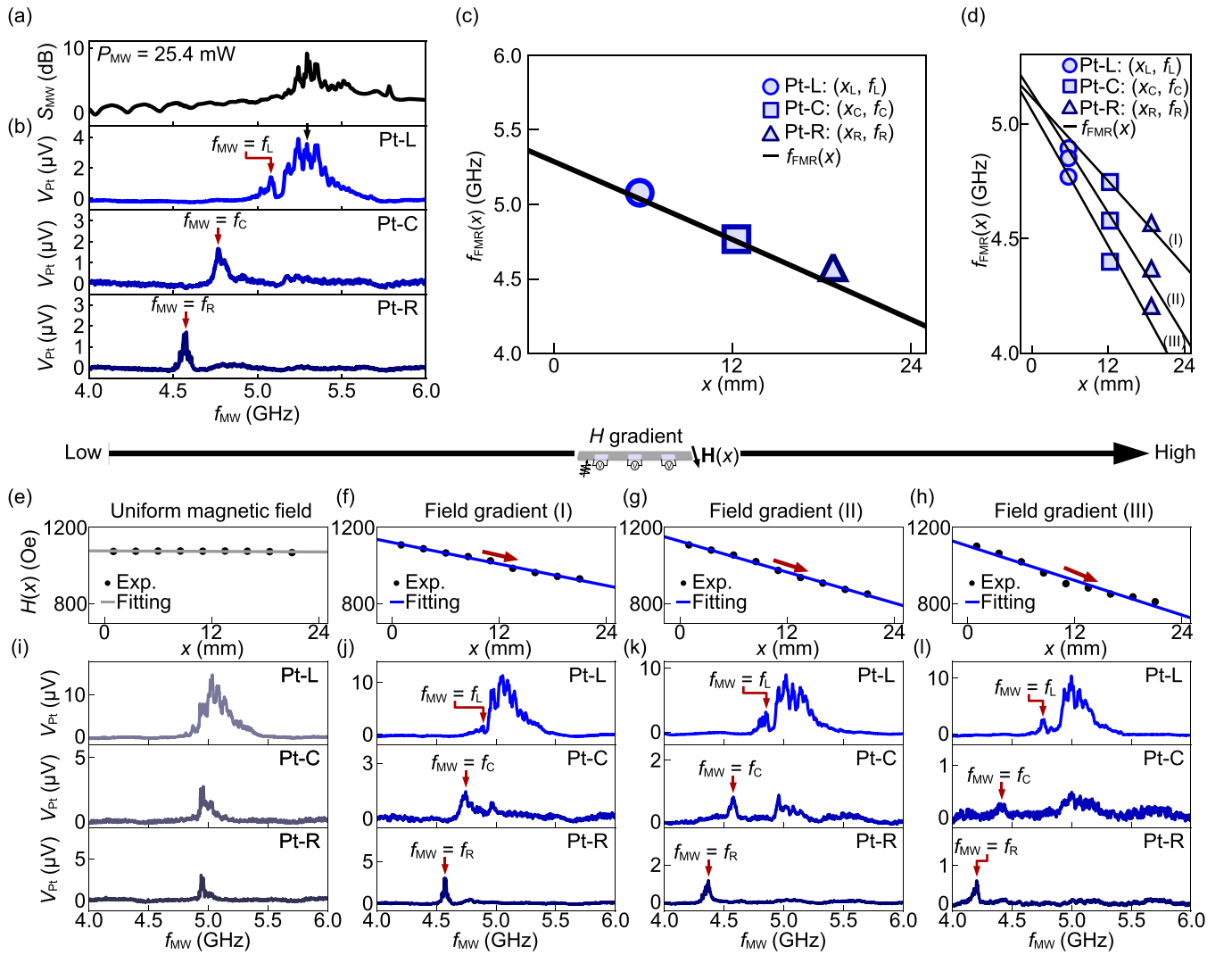
FIG. 3. (a) The f_{MW} dependence of the microwave absorption S_{MW}. (b) The f_{MW} dependence of V_{Pt} in each Pt film. The voltage peak appears at $f_{MW} = f_L$, f_C, and f_R in the Pt-L, Pt-C, and Pt-R films, respectively. (c) The x dependence of the ferromagnetic resonance (FMR) frequency of the YIG slab $f_{FMR}(x)$ (black solid line). The blue circle, rectangle, and triangle are the plots of (x_L, f_L), (x_C, f_C), and (x_R, f_R), respectively. (d) The x dependence of $f_{FMR}(x)$ in the magnetic-field gradients (I), (II), and (III). The plots of (x_L, f_L), (x_C, f_C), and (x_R, f_R) at each magnetic-field gradient are shown by blue circles, rectangles, and triangles, respectively. (e)–(h) The spatial dependence of the intensity of (e) a uniform magnetic field, (f) a magnetic-field gradient (I), (g) a field gradient (II), and (h) a field gradient (III). Experimental data and a linear fitting are shown by black plots and a solid line, respectively. (i)–(l) The f_{MW} dependence of V_{Pt} in each Pt film under (i) a uniform magnetic field, (j) a field gradient (I), (k) a field gradient (II), and (l) a field gradient (III). The value of P_{MW} was set to 25.1 mW in all measurements.
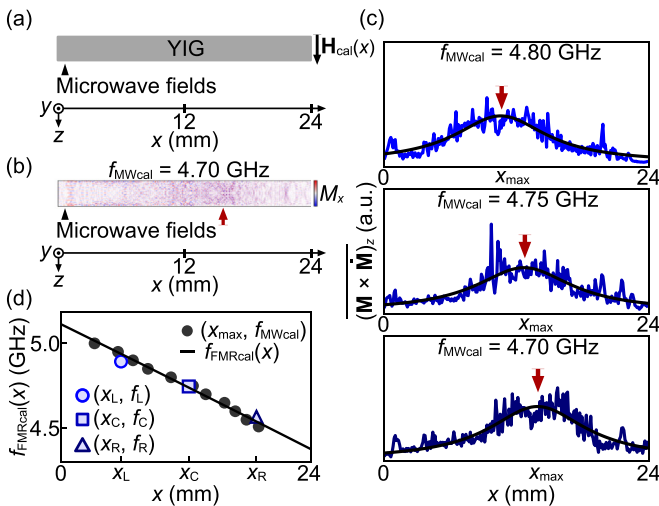
FIG. 4. (a) A schematic of the calculation setup. A magnetic field $\mathbf{H}_{cal}(x)$ with the amplitude $H_{cal}(x) \propto -x$ was applied in the z direction to a YIG slab. Microwave magnetic fields with the frequency f_{MWcal} were applied in the x direction to the left end of the YIG slab. (b) A snapshot of the spatial profile of M_x, the x component of magnetization $\mathbf{M}$, at $f_{MWcal} = 4.70$ GHz. (c) The x dependence of $\overline{(\mathbf{M} \times \dot{\mathbf{M}})_z}$, the z component of $\mathbf{M} \times \dot{\mathbf{M}}$ averaged about z and time, at $f_{MWcal} = 4.80$ GHz (upper panel), 4.75 GHz (middle panel), and 4.70 GHz (lower panel). A Lorentzian fitting is shown by a black solid curve, where x_{max} is the peak position of the Lorentzian function. (d) The x dependence of the FMR frequency in the calculation setup $f_{FMRcal}(x) = \frac{\gamma}{2\pi}\sqrt{[H_{cal}(x) - 4\pi N_z M_s][H_{cal}(x) - 4\pi N_z M_s + 4\pi M_s]}$ (black solid line). The f_{MWcal} dependence of x_{max} is plotted by black dots. The blue circle, rectangle, and triangle are the plots of (x_L, f_L), (x_C, f_C), and (x_R, f_R), respectively, in the field gradient (I) in the experiment.

f_{MWcal} [middle and upper panels in Fig. 4(c)], consistent with the experimental results on the V_{Pt} peaks at $f_{MW} = f_L, f_C$, and f_R [Fig. 3(b)]. As shown in Fig. 4(d), we confirmed that the detailed (x_{max}, f_{MWcal}) (black dots) agrees with Eq. (1) (black solid line) and the experimentally obtained value of (x_I, f_I) $(I = L, C, R)$ in the field gradient (I) (blue circle, rectangle, and triangle, respectively), showing that the excited spin wave is enhanced at the position where the spin wave satisfies the FMR condition. The agreement between the experimental results and the numerical calculation demonstrates that the observed voltage peaks originate from the spin pumping due to the nonlocal enhancement of propagating spin waves.

To summarize, we demonstrated nonlocal magnetic resonance in YIG exposed to nonuniform magnetic fields. The enhancement of the spin-wave ISHE voltage appears $\sim$ 18 mm distant from the spin-wave excitation position, showing that the spatial distribution of spin waves can be controlled by tuning external nonuniform magnetic fields. The observed results present possibilities of spintronics-based biomimetics as well as data processing.

[1] D. Geisler, *From Sound to Synapse: Physiology of the Mammalian Ear* (Oxford University Press, New York, 1998).

[2] H. Fletcher, Soc. Am. **23**, 637 (1951).

[3] D. D. Stancil and A. Prabhakar, *Spin Waves: Theory and Applications* (Springer, New York, 2009).

[4] S. Maekawa, S. O. Valenzuela, E. Saitoh, and T. Kimura, *Spin Current* (Oxford University Press, Oxford, 2012).

[5] Y. Kajiwara, K. Harii, S. Takahashi, J. Ohe, K. Uchida, M. Mizuguchi, H. Umezawa, H. Kawai, K. Ando, K. Takanashi, S. Maekawa, and E. Saitoh, Nature (London) **464**, 262 (2010).

[6] J. Holanda, D. S. Maior, A. Azevedo, and S. M. Rezende, Nat. Phys. **14**, 500 (2018).

[7] K. R. Smith, M. J. Kabatek, P. Krivosik, and M. Wu, J. Appl. Phys. **104**, 043911 (2008).

[8] Y. Cheng, A. J. Lee, G. Wu, D. V. Pelekhov, P. C. Hammel, and F. Yang, Nano Lett. **20**, 7257 (2020).

[9] See Supplemental Material at http://link.aps.org/supplemental/10.1103/PhysRevB.107.134408 for the details of the experimental results and the calculation setup.

[10] Y. Tserkovnyak, A. Brataas, and G. E. W. Bauer, Phys. Rev. Lett. **88**, 117601 (2002).

[11] S. Mizukami, Y. Ando, and T. Miyazaki, Phys. Rev. B **66**, 104413 (2002).

[12] A. Azevedo, L. H. Vilela Leão, R. L. Rodríguez-Suárez, A. B. Oliveira, and S. M. Rezende, J. Appl. Phys. **97**, 10C715 (2005).

[13] M. V. Costache, M. Sladkov, S. M. Watts, C. H. van der Wal, and B. J. van Wees, Phys. Rev. Lett. **97**, 216603 (2006).

[14] E. Saitoh, M. Ueda, H. Miyajima, and G. Tatara, Appl. Phys. Lett. **88**, 182509 (2006).

[15] K. Ando, Y. Kajiwara, S. Takahashi, S. Maekawa, K. Takemoto, M. Takatsu, and E. Saitoh, Phys. Rev. B **78**, 014413 (2008).

[16] K. Ando, T. An, and E. Saitoh, Appl. Phys. Lett. **99**, 092510 (2011).

[17] R. Iguchi, K. Ando, Z. Qiu, T. An, E. Saitoh, and T. Sato, Appl. Phys. Lett. **102**, 022406 (2013).

[18] A. Vansteenkiste, J. Leliaert, M. Dvornik, M. Helsen, F. Garcia-Sanchez, and B. Van Waeyenberge, AIP Adv. **4**, 107133 (2014).